

Tailoring (n,m) Structure of Single-Walled Carbon Nanotubes by Modifying Reaction Conditions and the Nature of the Support of CoMo Catalysts

Giulio Lolli, Liang Zhang, Leandro Balzano, Nataphan Sakulchaicharoen, Yongqiang Tan, and Daniel E. Resasco*

School of Chemical Biological and Materials Engineering, University of Oklahoma, 100 East Boyd Street, Norman, Oklahoma 73019

Received: October 24, 2005; In Final Form: December 13, 2005

The (n,m) population distribution of single-walled carbon nanotubes obtained on supported CoMo catalysts has been determined by photoluminescence and optical absorption. It has been found that the (n,m) distribution can be controlled by varying the gaseous feed composition, the reaction temperature, and the type of catalyst support used. When using CO as a feed over CoMo/SiO₂ catalysts, increasing the synthesis temperature results in an increase in nanotube diameter, without a change in the chiral angle. By contrast, by changing the support from SiO₂ to MgO, nanotubes with similar diameter but different chiral angles are obtained. Finally, keeping the same reaction conditions but varying the composition of the gaseous feed results in different (n,m) distribution. The clearly different distributions obtained when varying catalysts support and/or reaction conditions demonstrate that the (n,m) distribution is a result of differences in the growth kinetics, which in turn depends on the nanotube cap–metal cluster interaction.

1. Introduction

One of the most attractive features of single-walled carbon nanotubes (SWNT) is that their electronic properties strongly depend on their diameter and orientation of the carbon hexagons that form their walls. These characteristics are uniquely specified by the chiral vector identified with the integers (n,m), but most synthesis methods result in a wide distribution of (n,m) species.¹ If well-defined nanotube samples are desired, one can attempt to separate them on the basis of different affinities to functional groups or adsorbates. However, a more attractive approach would be the selective growth of specific nanotubes. Selective growth of SWNT has several meanings. In the first place, SWNT selectivity can imply the fraction of carbon in the sample forming SWNT as opposed to other forms of carbon. The second type of selectivity is regarding nanotube length, which, as recently shown, can only be controlled in some specific cases.² The third and more challenging type of selectivity is what can be called (n,m) selectivity, that is, the controlled production of specific (n,m) structures in much higher proportion than other structures.

The first type of selectivity is certainly highly desirable and determines the quality of SWNT. After years of effort, many groups are able now to produce samples of high SWNT selectivity, admittedly in small quantities. More recently, researchers have started to focus on the other two types of selectivity, which may have a great impact in the development of applications. Selective growth of nanotubes with well-specified structures (length, chirality) may greatly facilitate the construction of SWNT-based devices such as transistors, optoelectronic devices, photovoltaics, sensors, nanobiodetectors, etc.^{3–9} In general, a precise control of these properties will be crucial for any other application based on the uniqueness of the electronic properties of SWNT.^{10,11}

In previous work,^{12–15} we have demonstrated the ability of the CoMo catalysts used in our CoMoCAT process to achieve high selectivity of the first type (i.e., SWNT vs other forms of carbon). In this contribution, we will demonstrate that by varying operating conditions and catalyst substrate it is possible to vary the distribution of (n,m) species in the sample in a reproducible manner and with high specificity.

2. Experimental Section

2.1. Catalyst Preparation. Two catalyst formulations were investigated in this work, a 2 wt % CoMo/SiO₂ and a 0.3 wt % CoMo/MgO. (i) The silica-supported catalysts (2 wt % total metal, at a 1:3 and 2:1 Co/Mo molar ratio) were prepared by incipient wetness coimpregnation of an aqueous solution of (NH₄)₆Mo₇O₂₄·4H₂O and Co(NO₃)₂·6H₂O on SiO₂ (HiSil 210 from PPG). The impregnated material was dried in a convection oven at 110 °C for 12 h and then calcined at 500 °C for 3 h. (ii) The magnesia-supported catalysts had to be prepared by a different method due to the water solubility of the MgO support used (MgO from Alfa Aesar). The method employed is the so-called ethanol route described by Zdrzil et al.^{16,17} for the preparation of CoMo/MgO hydrodesulfurization catalysts. In this case, the same metal precursors and molar ratio (1:3) as used in the previous case were used. The total loading was reduced to 0.3% in order to accomplish the same loading-to-surface-area ratio. The resulting wet powder was then dried for 12 h at 110 °C and calcined at 500 °C as described above.

2.2. SWNT Growth. The nanotube synthesis was conducted in a vertically oriented fluidized bed quartz tube reactor of 20 mm inside diameter. The reactor had two quartz porous disks that kept the fluidized catalyst powder in the 100-mm-long reaction zone. To ensure constant temperature, the reactor was placed at the center of an electric furnace with a 300-mm-long heated zone. A thermocouple was mounted at the center of the heated zone and placed next to the quartz tube. About 5 g of catalyst were used in each run. The calcined catalyst was

* To whom correspondence should be addressed. Phone: (405) 325-4370. E-mail address: resasco@ou.edu.

prereduced in flowing H₂ (500 sccm) using a temperature ramp of 10 °C/min until the optimal reduction temperature was reached and held at that temperature for 30 min. The prereduction step is critical for the performance of the catalyst and can be optimized performing a temperature programmed reduction.¹⁸ The optimum temperature was determined for each support, 500 °C for SiO₂ and 350 °C for MgO. After the prereduction step, the reactor was purged using flowing He (1000 sccm), while the temperature was increased to the desired reaction temperature (700–850 °C). After the temperature was stabilized, the CO (or CH₄ for the 2:1 molar ratio catalysts) flow was started at a rate of 2000 sccm and kept for 30 min. At the end of the synthesis period, the reactor was purged with He (1000 sccm) and let cool to room temperature under He flow. The carbonyls in CO were eliminated by use of an A81 MaxiGaskleen Purifier, kindly donated by Pall Corp., Microelectronics.

2.3. SWNT Purification. In our production method, the SWNT product is recovered from the catalyst, particularly the support (silica or magnesia), which constitutes the majority of the material coming out of the reactor, by attacking the support with an appropriate solution. Silica is readily dissolved with a 10% HF solution under magnetic stirring for 10 min. Magnesia is easily dissolved in a 1.0 N solution of H₂SO₄. In each case, the resulting nanotubes were filtered and washed with deionized water until complete neutrality was reached. The wet material obtained on the filter was freeze dried to remove the excess water by sublimation, thus preserving the open structure typical of a nanotube web.

2.4. SWNT Suspensions. After the purification step, the nanotubes are still forming bundles and the optical properties of SWNT (optical absorption and fluorescence) are significantly affected by the state of aggregation. Therefore, to get a full identification of the types of nanotubes present in the sample, it is necessary to disperse the nanotubes as individual entities.^{19,20} Using surfactants and high energy sonication is an effective way of obtaining stable suspensions of individual SWNT in water. Moreover, Weisman et al.,^{21,22} using photoluminescence on HiPCO nanotubes suspended in SDS/D₂O solutions, have been able to assign experimental values for the S₁₁ and S₂₂ transitions for a large number of semiconducting nanotubes. These values have been corroborated by recent results obtained by Jorio et al.^{23–25} who used semicontinuous resonant Raman spectroscopy to cover a wide range of resonance energies. The availability of these values, which have some systematic differences with theoretical values¹¹ previously predicted on the basis of a simplified tight-binding approximation, has greatly facilitated the identification of individual (*n,m*) nanotube structures.

The surfactants most widely employed for this purpose have been sodium dodecyl sulfate (SDS)^{19–22} and sodium dodecyl benzene sulfonate (SDDBS).^{20,26} Another less frequently used surfactant that has been found to be even more effective than SDS and SDDBS in debundling the nanotubes is sodium cholate.^{27–29} Therefore, in this contribution, we have prepared stable surfactant suspensions by adding 2 mg of SWNT material to 20 mL of a 2 wt % aqueous solution of sodium cholate hydrate (from Sigma Aldrich). The suspension was placed under ultrasonic treatment by a horn sonic dismembrator (Model 500, Fisher Scientific) running at 30% power output for different times, typically 120 min. The resulting suspension was then ultracentrifuged (DuPont Sorvall SS-3) at 15 000 rpm (27 000 g) for 1 h to precipitate any residual particles and large aggregates of nanotubes.

2.5. SWNT (*n,m*) Analysis. The optical absorption equipment used in this study was a combination of a Bruker Equinox 55

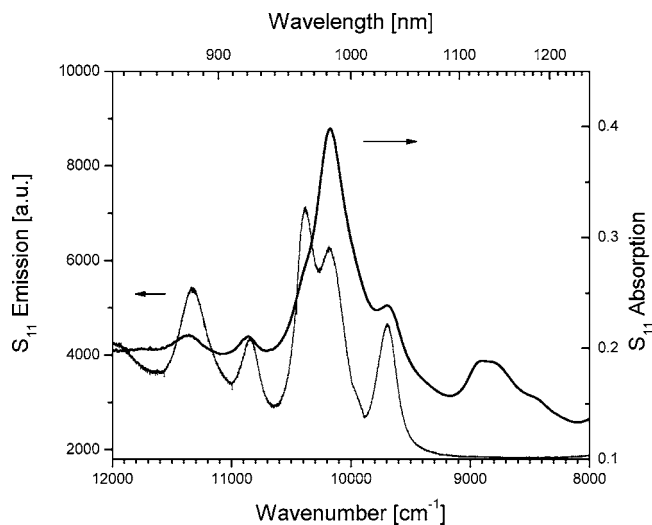


Figure 1. Superimposed emission and absorption spectra (S₁₁ region) for SWNT sample synthesized on CoMo/SiO₂ at 750 °C. Note that the emission bands are much better resolved than the absorption bands, but the relative intensities are greatly affected by the matching between the laser excitation energy and the S₂₂ absorption energy.

FTIR and a Shimadzu double-beam spectrometer UV-2101. A 10-mm light path “I” grade quartz cuvette was used for the measurements. Fluorescence spectra were obtained on a Jovin Yvon-Horiba LabRam 800 equipped with a charge-coupled device detector. The same “I” grade 10-mm path cell was used as sample holder. The laser excitation energy was 1.96 eV (633 nm).

To analyze the (*n,m*) distribution of individual nanotubes, we developed a protocol based on the combined use of optical absorption and fluorescence. The advantage of the fluorescence is its high sensitivity and its selectivity to isolated individual nanotubes, which results in a very high spectral resolution. However, this technique can only probe semiconducting nanotubes, and with only one laser excitation, the quantification of (*n,m*) species becomes complicated, as the intensity of the emission strongly depends on how far is the absorption energy from the excitation energy (1.96 eV in this case). On the other hand, optical absorption can probe both metallic and semiconducting nanotubes, and in a first approximation, it can be considered quantitative if the same absorption extinction coefficients are assumed for every (*n,m*) nanotube. The disadvantage of this technique is that it generally exhibits broader and less resolved peaks, which makes (*n,m*) identification more difficult.

The comparison of the two techniques is made in Figure 1, in which we show the absorption and emission spectra of a suspension of SWNT produced at 750 °C on the CoMo/SiO₂ catalyst using CO as feed. The intensity of individual peaks in the emission spectra are greatly affected by how close the energy of the exciting laser is to the S₂₂ transition. Therefore, working with only one laser, the observed intensities are not directly related to the (*n,m*) population. This effect is clearly illustrated for the case of the (8,3) nanotube; its S₂₂ transition occurs at 1.86 eV, which is very close to the excitation energy. This resonance greatly enhances the intensity of the emission band. However, as shown below, the actual amount of (8,3) in the sample is very small. At the other extreme, the (6,5) nanotube that is the most abundant species in this sample has its S₂₂ transition at an energy of 2.19 eV, far removed from the excitation energy. As a result, the emission band is greatly reduced.

The most accurate technique for probing semiconducting nanotubes, as used by Weisman et al.,^{21,22} would be to use a

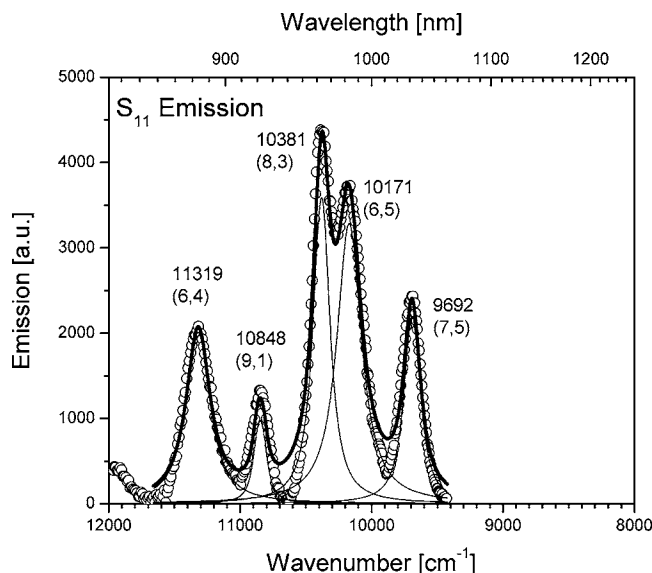


Figure 2. Fitting of the S_{11} emission spectrum for SWNT sample synthesized on CoMo/SiO₂ at 750 °C. Constrained fwhh = 148.0 ± 2.6, $R^2 = 0.949$.

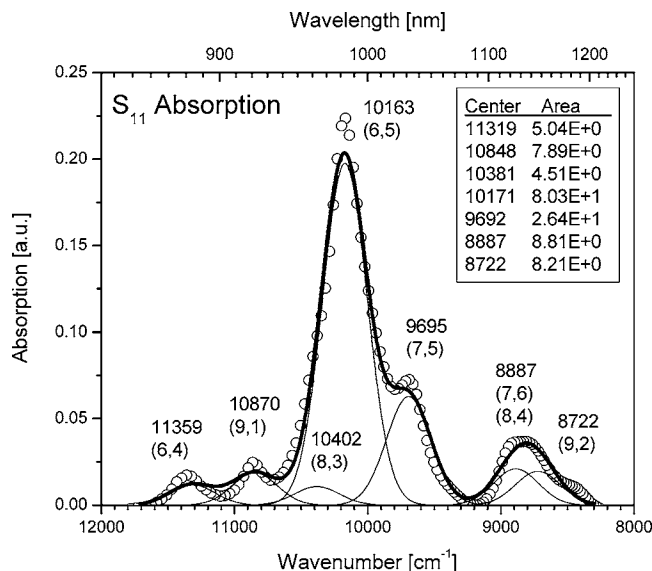


Figure 3. Fitting of the S_{11} absorption spectrum for SWNT sample synthesized on CoMo/SiO₂ at 750 °C. Constrained fwhh = 328.5 ± 1.1, $R^2 = 0.989$.

semi-continuous-laser-excitation photoemission and find the resonance energy for each nanotube. This method combines the photoluminescence resolution with a quantitative measurement of the (n,m) population distributions. However, not having available a laser with semicontinuous excitation energy, we have combined the photoluminescence and optical absorption techniques to fully characterize the nanotubes in our sample. First, we use the fluorescence S_{11} emission spectra (see Figure 2) to individualize all the semiconducting nanotubes present in the sample and to determine the exact position of the S_{11} transition. This is necessary because, as shown by Bachilo et al.,^{21,22} the environment around the nanotube creates a red shift in the optical transition. When surfactants with different molecular weights and strength of interaction with the nanotube surface were compared, different extents of red shift (ranging from 20 to 60 cm^{-1}) were observed.^{21,22,30,31}

Second, by use of the peak position of each semiconducting nanotube identified in fluorescence, it is possible to fit the optical absorption S_{11} region revealing even the smallest shoulders that

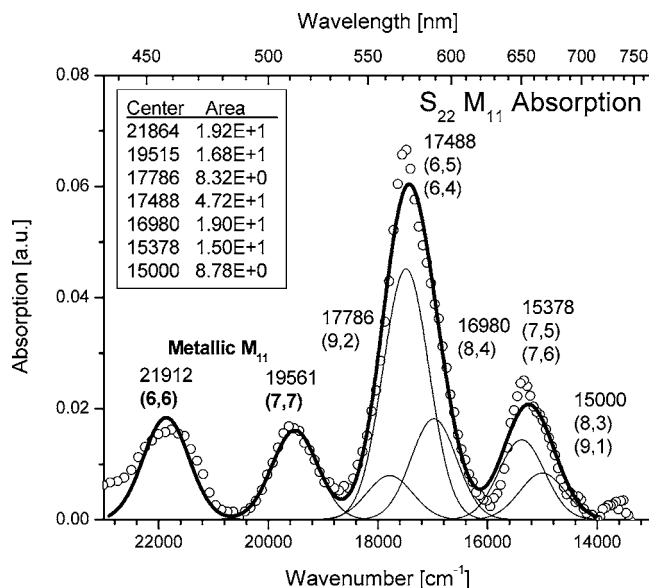


Figure 4. Fitting of the S_{22} and M_{11} region for SWNT sample synthesized on CoMo/SiO₂ at 750 °C. Constrained fwhh = 815.0 ± 12, $R^2 = 0.975$.

TABLE 1: Estimated Population on Different Catalysts and Different Reaction Conditions from the Analysis of the M_{11} , S_{22} , and S_{11} Optical Absorption of the Samples

	support		SiO ₂				MgO
		temp (°C)	700	750	800	850	750
(n,m) species	semicond	(6,5)	54%	42%	55%	6%	19%
		(8,4)	4%	16%	4%	6%	12%
		(7,5)	8%	8%	6%	10%	26%
		(7,6)	8%	7%	6%	15%	13%
	metallic	(8,6)			1%	10%	2%
		(8,7)			2%	13%	2%
		(6,6)	14%	19%	15%	17%	22%
		(7,7)	13%	10%	10%	14%	3%
						6%	

otherwise would have been difficult to reveal (Figure 3). The best fit was obtained using a Levenberg–Marquardt routine. From this fitting it is possible to estimate an (n,m) distribution from the S_{11} . Then, starting from these data and the average red shift, we fitted the S_{22} absorption region. The remaining peaks in this region that cannot be attributed to any semiconducting nanotube should be found among the metallic nanotubes M_{11} , as illustrated in Figure 4. To obtain a quantitative estimation of the population, the fittings were conducted using a sum of Gaussians with the same bandwidth to minimize the number of fitting parameters. The width was constrained to the value of the strongest band. The constraint on the width, even when it reduces the overall quality of the fittings by using less fitting parameters, provides a more realistic (n,m) population distribution. The uncertainty in the calculated nanotube distribution arises from the overlap of some transitions. For example, the presence of the (6,4) nanotube in small amounts is evident from both the emission and absorption spectra. However it's S_{22} transition overlaps with that of the most abundant (6,5), which affects the final fitting. Other uncertainties are associated with the assignment of the metallic nanotubes, for which only theoretical¹¹ or semiempirical values^{23–25} of their position in the spectrum are available.

3. Results and Discussion

The narrow distribution of diameters and chiralities in the CoMoCAT sample prepared at 750 °C in CO on the CoMo/

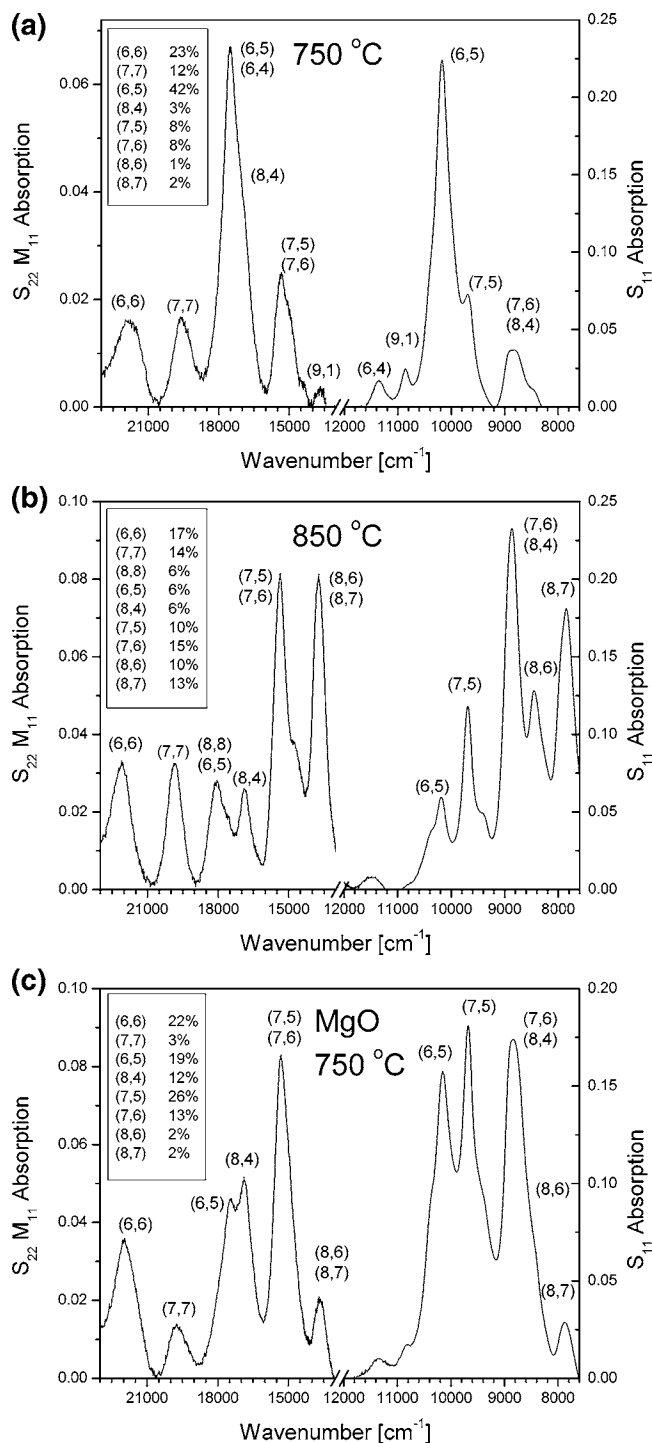


Figure 5. (a) (n,m) assignments for the SWNT sample synthesized CoMo/SiO₂ at 750 °C. (b) (n,m) assignments for the SWNT sample synthesized CoMo/SiO₂ at 850 °C. (c) (n,m) assignments for the SWNT sample synthesized CoMo/MgO at 750 °C.

SiO₂ catalyst has been previously reported and recently corroborated in several laboratories.^{32–36} In this contribution, we demonstrate that, by varying the temperature of operation as well as the substrate on which the CoMo particles are supported, one can modify the distribution of (n,m) nanotubes in a reproducible manner. It is important to emphasize the point of reproducibility. During the last two years, we have been able to reproducibly obtain SWNT samples with exactly the same (n,m) distribution when the catalyst formulation and reaction conditions were kept unchanged.

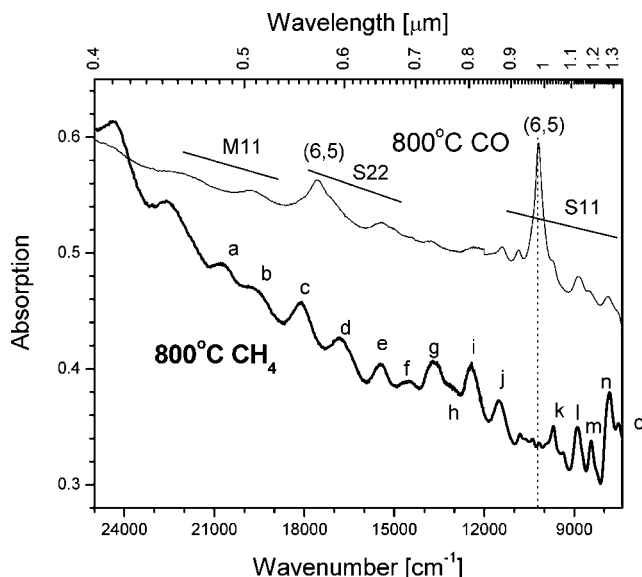


Figure 6. Top (800 °C CO): Note that (6,5) constitutes the majority of the nanotubes present (the spectrum has been shifted for the sake of clarity). Bottom (800 °C CH₄): Note the broader nanotube distribution. M₁₁ {a, b, and c}; S₂₂ {d (8,4), e (7,5) (7,6), f (12,2), g (8,6) (8,7), h (10,6), i (12,1), and j (14,0) (11,6) (13,2) (12,4)}; S₁₁ {k (7,5), l (8,4) (7,6), m (12,1) (8,6), n (8,7), and o (12,4) (13,2)}. The (14,0) and (11,6) for which S₂₂ was observed have their S₁₁ outside the detection limit of the instrument.

3.1. Effect of Synthesis Temperature. By use of the same CoMo 1:3 SiO₂-supported catalyst described above, we varied the synthesis temperature in the range 700–850 °C. Above 850 °C the silica used as support started sintering, resulting in low carbon yields. Parts a and b of Figure 5 summarize the S₁₁/S₂₂/M₁₁ spectra of the nanotubes produced on the SiO₂-supported catalysts at increasing temperatures using CO. Table 1 summarizes the nanotube distributions obtained by fitting the spectra recorded for several intermediate temperatures that for the sake of conciseness are not shown here. As we have previously shown,^{33,37} the diameter of the nanotubes increases as the reaction temperature increases. Here, we have monitored this change at the (n,m) level. As shown in parts a and b of Figure 5, the nanotube distribution shifts from a dominant (6,5) at the low-temperature end (700–750 °C) to (7,6) and to (8,7) at 850 °C. Interestingly, the nanotube diameter increases with temperature, but the chiral angle stays close to the armchair line (see the (n,m) map in Figure 7). We have previously explained the increase in diameter with temperature in terms of a faster rate of metal agglomeration at higher temperatures that cause a shift to larger diameter caps during the nucleation that precedes the nanotube growth.^{33,37}

The narrow distribution in chiral angle deserves some discussion. If one examines the edge of the cap of an armchair nanotube, one can see a regular array of atoms. It has been demonstrated³⁸ that, when coordinated to a metal surface, such a regular array forms a more stable structure than the cap of a chiral nanotube. Specifically, when one compares the cap of the (6,6) nanotube to that of the (6,5) on a Ni surface, there is a small difference in stability in favor of the armchair nanotube.³⁸ However, as shown in the present contribution, on the low-temperature samples, the amount of (6,5) is much higher than that of (6,6). This result demonstrates that, to explain the population of a given nanotube sample, one should use kinetic rather than thermodynamic considerations. Accordingly, the preferred growth of (6,5) nanotubes might suggest that within the nanotubes of this specific diameter (determined by the cluster

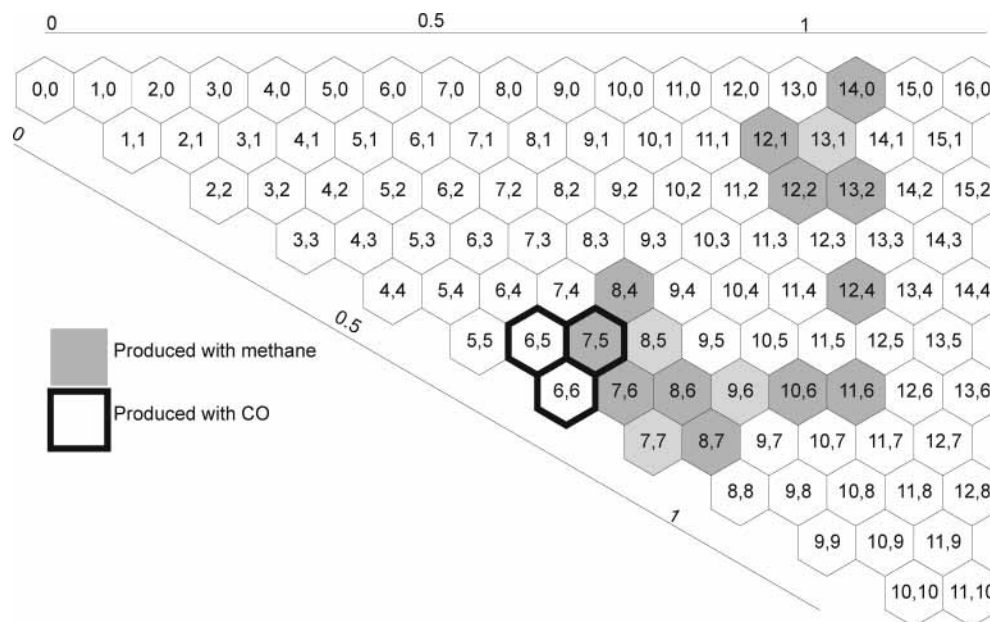


Figure 7. (n,m) map, effect of gas feed at 800 °C on the produced SWNT. Nanotube diameters are indicated for 0, 0.5, and 1.0 nm.

size), the growth of this specific nanotube has the lowest (kinetic) activation energy.

Miyauchi et al.³⁹ have observed similar preferential tendency to high-angle chirality in nanotube samples prepared by decomposition of ethanol. They have indicated that this preference is particularly pronounced when the nanotube diameter is small, as is the case of the SWNT produced by the CoMoCAT method. It is conceivable that the activation energy for growth varies from tube type to tube type much more pronouncedly when the nanotube diameter is small and that difference in energy becomes much smaller as the (n,m) integers increase. We have observed this effect on our catalyst running the reaction with methane.

3.2. Effect of Gas Feed. Varying the carbon-containing gaseous feed from CO to CH₄ provides another interesting comparison. The CO disproportionation is exothermic, while the dehydrogenative decomposition of CH₄ is endothermic. Therefore, while the former is limited by equilibrium at the high temperatures needed for nanotube growth, the latter is not. In addition, while the byproduct of CH₄ decomposition is a reducing agent (H₂), that from CO disproportionation is oxidizing (CO₂). As a result, one should expect different kinetic behavior, and consequently different (n,m) selectivity, even when the reaction temperature is kept constant. Indeed, this difference is illustrated in Figure 6 with the UV–vis–NIR spectra of the SWNT produced at 800 °C from CH₄ and from CO. Clearly, CH₄ is less (n,m) selective than CO at this temperature. This can be explained by the same surface energetics arguments mentioned above. The nanotubes produced in this case are of larger diameter and with a broader distribution than those obtained with CO. This larger diameter can be linked to the evolution of hydrogen, a byproduct of the CH₄ decomposition reaction. As we have previously shown, hydrogen has a dual effect during the nucleation of carbon and formation of the nanotube cap. It not only increases the rate of reduction and sintering of metal clusters, but it also hinders the nucleation of carbon species on the surface of the cluster by decreasing the carbon surface fugacity, a well-known phenomenon in heterogeneous catalysis.^{40,41} As a result, the formation of the cap occurs at a larger size. That is, with CH₄ as a feed, the size of the metal cluster are not only determined by the CoMo interaction, but also by the extent of CH₄ conversion, which in

turns varies the catalyst exposure to H₂. Because the concentration of H₂ is a function of conversion, it varies throughout the bed, causing a broad distribution of metal cluster sizes and consequently nanotube diameters that range from 0.8 to 1.3 nm, contrasting with the narrow range obtained with CO. Moreover, as noted by Miyauchi et al. in the case of nanotubes produced by ethanol disproportionation,³⁹ the differences in the thermodynamic stability of small diameter nanotubes are more pronounced compared to those of large diameters. In the chirality map of Figure 7, we can clearly observe that, when the nanotubes are produced with very small diameters, they appear very close to the armchair line. By contrast, when they have diameters above 1 nm they appear near both the zigzag and armchair lines, and at even larger diameters they distribute to an even broader range of chiral angles. Clearly, the CH₄ feed does not result in such a narrow (n,m) distribution as the CO feed does.

To further investigate the role of H₂ in determining the diameter distributions we co-fed 1% H₂ in the CO feed at 750 °C. The optical absorption spectrum is compared in Figure 8 with that of the sample obtained on the same catalyst in the absence of H₂. As we can clearly see, the addition of H₂ broadens the diameter distribution toward larger diameters. This confirms the role of hydrogen in lowering the carbon fugacity on the cluster surface, thus delaying the nucleation of the cap. If during this delay the cluster continues growing by metal sintering, the formation of the cap will occur at a larger diameter. Therefore, the nanotube that results will have a larger diameter, as we have previously suggested.¹⁵ The effect of H₂ addition, if done in a controlled way, can help and enhance the effect of increasing temperature in determining the diameter distribution of nanotubes. Thus, compared to the reaction using CH₄, a mixture CO/H₂ results in narrower diameter distribution.

3.3. Effect of Catalyst Support. From the above results, it appears that high (n,m) selectivity can only be accomplished at small diameters and at chiral angles near the armchair line ($n = m$). The question is whether one can obtain with some selectivity nanotubes with a given diameter but different chiral angles. We have attempted to accomplish this by modifying the morphology of the metal cluster via an interaction with the support. It is well known in the field of heterogeneous catalysis that the catalyst support plays a more relevant role than simply providing a high surface area to stabilize small particles.⁴² In

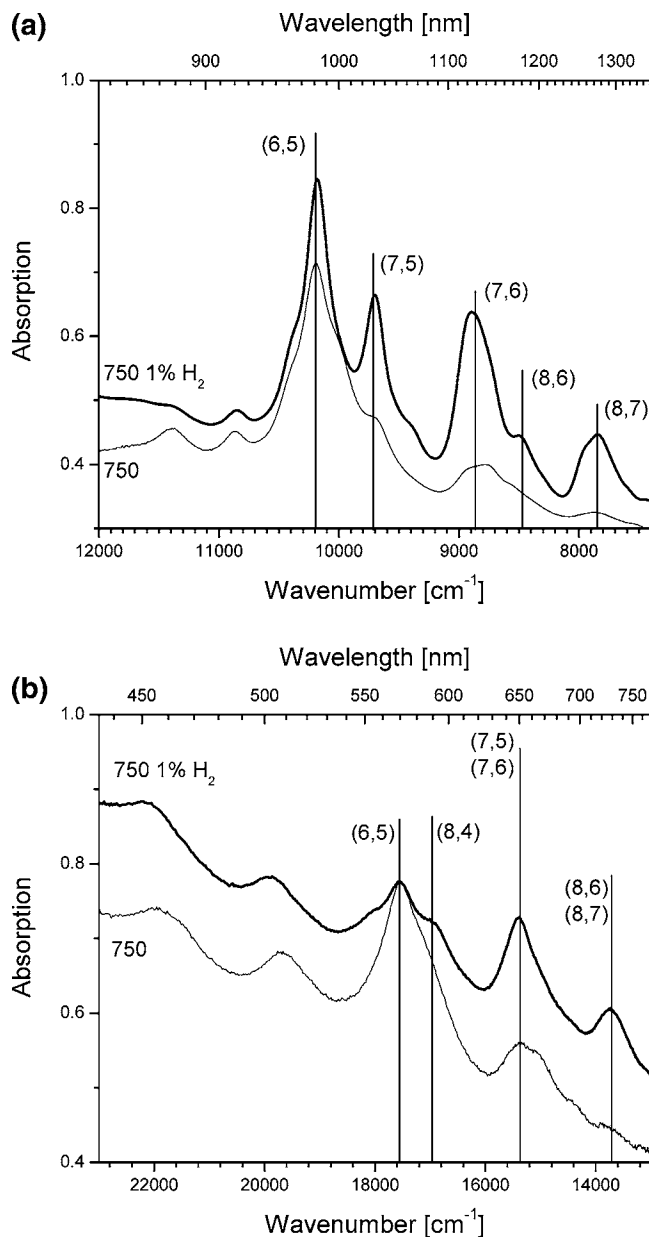


Figure 8. (a) Optical absorption spectra (S_{11} region) of nanotubes produced on the same CoMo/SiO₂ catalyst at 750 °C, with different feeds. Top, CO/1% H₂; bottom, pure CO. (b) Optical absorption spectra (S_{22} region) of nanotubes produced on the same CoMo/SiO₂ catalyst at 750 °C, with different feeds. Top, CO/1% H₂; bottom, pure CO.

fact, by varying the nature of this stabilization, some times termed “metal–support interaction,” one can cause changes in the morphology of the small metal and/or oxide clusters supported on the high surface area oxide.

To vary the morphology of the metal clusters involved in the reaction, we changed the type of support used to stabilize the active particles. We compared SiO₂ and MgO. The former exhibits low strength of interaction with the active species. The latter is known to interact strongly with Mo and to form solid solutions with Co ions. The expected surface morphology is a highly dispersed metal oxide phase. In fact, the degree of dispersion can be evaluated using diffusive reflectance spectroscopy. The band energy gap is directly related to the metal oxide domain size. In previous work it has been recommended to use the square root of the Kubelka–Munk function multiplied by the photon energy and plot this new function versus the photon energy.⁴³ By application of this method to the spectral

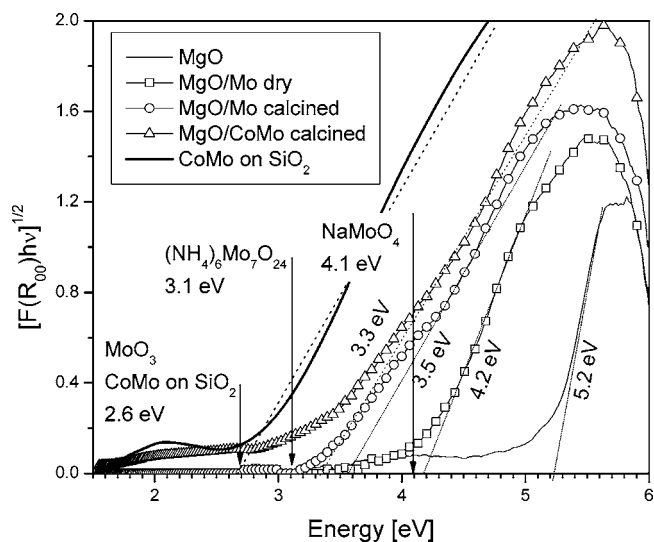


Figure 9. Diffusive reflectance band-gap extrapolation for the MgO supported catalyst and SiO₂ catalysts. Gaps for reference compounds are marked.

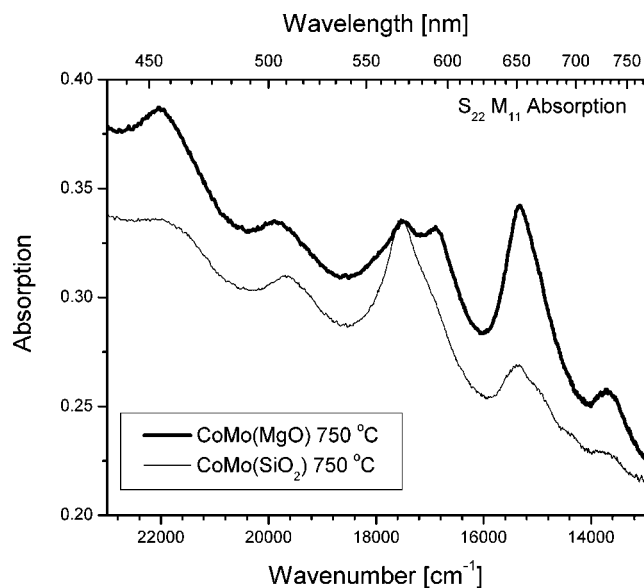


Figure 10. Optical absorption spectra ($M_{11} S_{22}$ region) of nanotubes produced at 750 °C with pure CO on MgO- and SiO₂-supported catalysts.

data shown in Figure 9, we have estimated the gap energy for the MgO-supported catalyst during various stages of the production. Energy gaps of compounds with known domain size are added as reference. This analysis demonstrates that the MgO-supported catalyst has a very small domain size during all the stages. While the main increase in domain size is caused by the first calcinations step, the final catalyst has a band gap of 3.3 eV, which lies between that of the isolated molybdate (MoO_4^-) species and the paramolybdate ($\text{Mo}_7\text{O}_{24}^{6-}$), which is also a highly dispersed species. By contrast, the SiO₂-supported catalyst shows a band gap of 2.6 eV, close to the value of bulk crystalline MoO₃, which indicates that the Mo species over the two supports have different morphologies. It is expected that the CoMoO_x clusters on the MgO are much more disordered than the ones found on SiO₂.

This difference in surface morphology leads to the growth of different SWNTs. In fact, as shown in Figure 10, the UV–vis spectra of SWNT produced on MgO- and SiO₂-supported catalysts at the same temperature (750 °C) and reaction

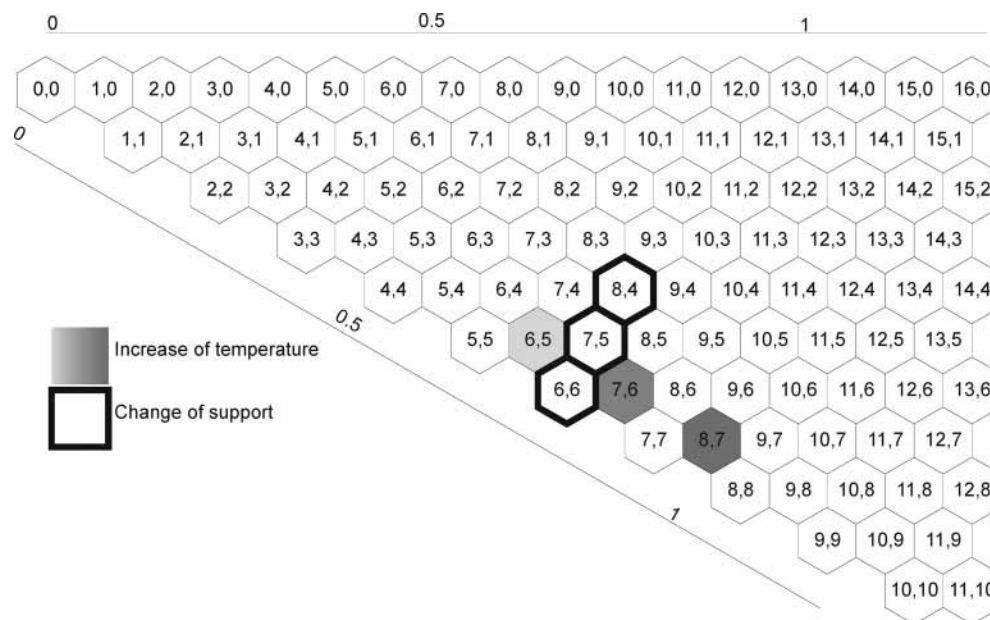


Figure 11. (n,m) map, effect of temperature and support morphology on the produced SWNT. Nanotube diameters are indicated for 0, 0.5, and 1.0 nm.

conditions are significantly different. The (n,m) assignments for the two products are compared in parts a and c of Figure 5; the one from the MgO support has less (6,5) and more (7,5), (8,4), and (6,6). Interestingly, the average diameter is similar for the four nanotube types, but the chiral angle is reduced in the MgO sample. These results are summarized in the (n,m) map of Figure 11. The observed trends indicate that the catalysts support, the temperature, and the gas composition are parameters that one can adjust to vary the chiral angle and diameter of the nanotubes in a reproducible way.

4. Conclusions

In summary, we have found that using a highly selective CoMo catalyst the (n,m) distribution of the SWNT product can be reproducibly altered by varying the reaction temperature, the gaseous feed, or the cluster surface morphology. The main effect of increasing the reaction temperature is to increase the metal particle size during the SWNT growth and consequently the nanotube diameter. The temperature effect can be enhanced adding directly or indirectly H_2 in the system. The presence of hydrogen decreases the rate of carbon nucleation, while the metallic clusters continue agglomerating. As a result, the late nucleation results in larger caps and consequently nanotubes of larger diameter. By varying the support one affects the resulting morphology of the metal cluster, and as a result, the chiral angle of the nanotube produced. This effect can be explained in terms of the energetics of the nanotube caps and the kinetics of their formation. The cap of a chiral tube is more distorted compared to that of an armchair (30°) or zigzag tube (0°). This difference is particularly pronounced in the case of small-diameter nanotubes but becomes less important as the SWNT diameter increases. As a result, it is more difficult to have (n,m) control with larger diameter nanotubes. Finally, the interaction of the metal and the support plays an important role in the size and morphology of the cluster. The production of nanotubes with larger chiral angle, i.e., more distorted caps, would indicate that a more distorted metallic cluster is stabilized on the MgO support than on the SiO_2 support. By the appropriate selection of the growth parameters (support, gas, temperature, etc.) one can have a relatively narrow control of the (n,m)

distribution. This (n,m) selectivity provides a remarkable tool for tailoring specific nanotubes without the need of post-growth separation methods.

Acknowledgment. Financial support from DoE Basic Energy Sciences (Grant No. DE-FG03-02ER15345) and NSF Grant No. CTS-0308619 is gratefully acknowledged.

References and Notes

- (1) Henrard, L.; Bernier, P.; Journet, C.; Loiseau, A. *Synth. Met.* **1999**, *103*, 2533.
- (2) Maruyama, S.; Einarsson, E.; Murakami, Y.; Edamura, T. *Chem. Phys. Lett.* **2005**, *403*, 320.
- (3) Baughman, R. H.; Zakhidov, A. A.; de Heer, W. A. *Science* **2002**, *297*, 787.
- (4) Peng S.; Cho K.; Qi P.; Dai H. *Chem. Phys. Lett.* **2004** *387*, 271.
- (5) Kong, J.; Franklin, N.; Zhou, C.; Chapline, M.; Peng, S.; Cho, K.; Dai, H. *Science* **2000**, *287*, 622.
- (6) Kymakis, E.; Alexandrou, I.; Amaratunga, G. A. J. *J. Appl. Phys.* **2003**, *93*, 1764.
- (7) Yakobson, B. I.; Smalley, R. E. *Recherche* **1998**, *307*, 50.
- (8) Kazaoui, S.; Minami, N.; Nalini, B.; Kim, Y.; Takada, N.; Hara, K. *Appl. Phys. Lett.* **2005**, *87*, DOI: 10.1063/1.2136435.
- (9) Kazaoui, S.; Minami, N.; Nalini, B.; Kim, Y.; Hara, K. *J. Appl. Phys.* **2005**, *98*, DOI: 10.1063/1.2113419.
- (10) Dresselhaus, M. S.; Eklund, P. C. *Adv. Phys.* **2000**, *49*, 705.
- (11) Kataura, H.; Kumazawa, Y.; Maniwa, Y.; Umez, I.; Suzuki, S.; Ohtsuka, Y.; Achiba, Y. *Synth. Met.* **1999**, *103*, 2555.
- (12) Alvarez, W. E.; Kitiyanan, B.; Borgna, A.; Resasco, D. E. *Carbon* **2001**, *39*, 547.
- (13) Herrera, J. E.; Resasco, D. E. *J. Catal.* **2004**, *221*, 354.
- (14) Resasco, D. E.; Alvarez, W. E.; Pompeo, F.; Balzano, L.; Herrera, J. E.; Kitiyanan, B.; Borgna, A. *J. Nanopart. Res.* **2002**, *4*, 131.
- (15) Resasco, D. E.; Herrera, J. E.; Balzano, L. *J. Nanosci. Nanotechnol.* **2004**, *4*, 398.
- (16) Zdrzil, M. *Catal. Today* **2001**, *65*, 301.
- (17) Zdrzil, M. *Catal. Today* **2003**, *86*, 151.
- (18) Herrera, J. E.; Balzano, L.; Borgna, A.; Alvarez, W. E.; Resasco, D. E. *J. Catal.* **2001**, *204*, 129.
- (19) Karachevtsev, V. A.; Glamazda, A. Yu.; Dettlaff-Weglikowska, U.; Leontiev, V. S.; Plokhotnichenko, A. M.; Roth, S. *AIP Conf. Proc.* **2003**, *685*, 202.
- (20) Moore, V. C.; Strano, M. S.; Haroz, E. H.; Hauge, R. H.; Smalley, R. E.; Schmidt, J.; Talmon, Y. *Nano Lett.* **2003**, *3*, 1379.
- (21) Bachilo, S. M.; Strano, M. S.; Kittrell, C.; Hauge, R. H.; Smalley, R. E.; Weisman, R. B. *Science* **2002**, *298*, 2361.

- (22) O'Connell, M. J.; Bachilo, S. M.; Huffman, C. B.; Moore, V. C.; Strano, M. S.; Haroz, E. H.; Rialon, K. L.; Boul P. J.; Noon, W. H.; Kittrell, C.; Ma, J.; Hauge, R. H.; Weisman, R. B.; Smalley, R. E. *Science* **2002**, *297*, 593.
- (23) Jorio, A.; Santos, A. P.; Ribeiro, H. B.; Fantini, C.; Souza, M.; Vieira, J. P. M.; Furtado, C. A.; Jiang, J.; Saito, R.; Balzano, L.; Resasco, D. E.; Pimenta, M. A. *Phys. Rev. B* **2005**, *72*, 75207.
- (24) Jorio, A.; Fantini, C.; Pimenta, M. A.; Capaz, R. B.; Samsonidze, Ge.G.; Dresselhaus, G.; Dresselhaus, M. S.; Jiang, J.; Kobayashi, N.; Gruneis, A.; Saito, R. *Phys. Rev. B* **2005**, *71*, 75401.
- (25) Fantini, C.; Jorio, A.; Souza, M.; Strano, M. S.; Dresselhaus, M. S.; Pimenta, M. A. *Phys. Rev. Lett.* **2004**, *93*, 147406.
- (26) Matarredona, O.; Rhoads, H.; Li, Z.; Harwell, J. H.; Balzano, L.; Resasco, D. E. *J. Phys. Chem. B* **2003**, *107*, 13357.
- (27) Tan, Y.; Resasco, D. E. *J. Phys. Chem. B* **2005**, *109*, 14454–14460.
- (28) Hertel, T.; Hagen, A.; Talalaev, V.; Arnold, K.; Hennrich, F.; Kappes, M.; Rosenthal, S.; McBride, J.; Ulbricht, H.; Flahaut, E. *Nano Lett.* **2005**, *5*, 511.
- (29) Wenseleers, W.; Vlasov, I. I.; Goovaerts, E.; Obraztsova, E. D.; Lobach, A.; Bouwen, A. *Adv. Funct. Mater.* **2004**, *14*, 1105.
- (30) Jorio, A.; Fantini, C.; de Souza, M.; Saito, R.; Samsonidze, Ge. G.; Dresselhaus, G.; Dresselhaus, M. S.; Pimenta, M. A. *AIP Conf. Proc.* **2004**, *723*, 157.
- (31) Saito, R.; Gruneis, A.; Jiang, J.; Jorio, A.; Cancado, L. G.; Fantini, C.; Pimenta, M. A.; Samsonidze, Ge. G.; Dresselhaus, G.; Dresselhaus, M. S.; Souza Filho, A. G. *AIP Conf. Proc.* **2004**, *723*, 407.
- (32) Resasco, D. E.; Balzano, L.; Herrera, J. E.; Matarredona, O.; Zheng, L. *AIP Conf. Proc.* **2004**, *723*, 27.
- (33) Zhang, L.; Balzano, L.; Resasco, D. E. *J. Phys. Chem. B* **2005**, *109*, 14375.
- (34) Bachilo, S. M.; Balzano, L.; Herrera, J. E.; Pompeo, F.; Resasco, D. E.; Weisman, R. B. *J. Am. Chem. Soc.* **2003**, *125*, 11186.
- (35) Chou, S. G.; Ribeiro, H. B.; Barros, E. B.; Santos, A. P.; Nezhich, D.; Samsonidze, Ge.G.; Fantini, C.; Pimenta, M. A.; Plentz Filho, F.; Dresselhaus, M. S.; Dresselhaus, G.; Saito, R.; Zheng, M.; Onoa, G. B.; Semke, E. D.; Swan, A. K.; Unlu, M. S.; Goldberg, B. B. *Chem. Phys. Lett.* **2004**, *397*, 296.
- (36) Hennrich, F.; Krupke, R.; Lebedkin, S.; Arnold, K.; Fischer, R.; Resasco, D. E.; Kappes, M. M. *J. Phys. Chem. B* **2005**, *109*, 10567.
- (37) Resasco, D. E.; Herrera, J. E.; Balzano, L. *J. Nanosci. Nanotechnol.* **2003**, *3*, 1.
- (38) Robertson, J.; Li, L.; Reich, S. *NASA/Rice 2nd Workshop on SWNT Nucleation and Growth Mechanisms*, **2005**.
- (39) Miyauchi, Y.; Chiashi, S.; Murakami, Y.; Hayashida, Y.; Maruyama, S. *Chem. Phys. Lett.* **2004**, *387*, 198.
- (40) Boudart, M. *Catal. Lett.* **1989**, *3*, 111.
- (41) Iglesia, E.; Baumgartner, J. E.; Price, G. L. *J. Catal.* **1992**, *134*, 549.
- (42) Haller, G. L.; Resasco, D. E. *Adv. Catal.* **1999**, *36*, 173.
- (43) Barton, D. G.; Shtein, M.; Wilson, R. D.; Soled, S. L.; Iglesia, E. *J. Phys. Chem. B* **1999**, *103*, 630–640.